International Forum on Aeroelasticity and Structural Dynamics
IFASD 2017
25-28 June 2017 Como, Italy

EXPERIMENTAL AND NUMERICAL INVESTIGATION OF POST-FLUTTER LIMIT CYCLE OSCILLATIONS ON A CANTILEVERED FLAT PLATE

Kiran Ramesh[1], Tiago Priolli Monteiro[2], Flávio José Silvestre[2], Antônio Bernardo Guimarães Neto[2], Thiago de Souza Siqueira Versiani[2], Roberto Gil Annes da Silva[2]

[1]Aerospace Sciences Division,School of Engineering
University of Glasgow
Glasgow, UK, G12 8QQ
kiran.ramesh@glasgow.ac.uk

[2]Divisão de Engenharia Aeronáutica
Instituto Tecnológico de Aeronáutica
12228-900 São José dos Campos, Brazil
tiago.priolli@gmail.com
flaviojs@ita.br
antoniobgn@gmail.com
versiani.t@gmail.com
gil@ita.br

Keywords: flexible wings, leading edge vortices, HALE, cantilevered plate, fluid structure interaction

Abstract:

Futuristic aircraft designs and novel aircraft such as High Altitude Long Endurance (HALE) involve a higher level of structural flexibility than in conventional aircraft. Even at present, the trends in the aviation industry are to increase wing length (to reduce induced drag) and maximize use of composites, which lead to increased structural flexibility. This necessitates a rethink of conventional (linear) aeroelastic analysis, since the increased flexibility results in coupling between the flight dynamic and aeroelastic dynamics, and consequently, limit-cycle oscillations of the structure. In this paper, a new three-dimensional low-order model for unsteady aerodynamics that accounts for large oscillation amplitudes and nonplanar wakes is developed. An experiment with a cantilevered flat plate at low Reynolds number is set up and used to validate the low-order model, as well as to study post-flutter limit-cycle oscillations. Results from the low-order model are promising, but show that aerodynamic nonlinearities such as flow separation and leading-edge vortex shedding must also be modeled in order to predict all possible limit-cycle oscillations of the aeroelastic system.

1 INTRODUCTION

Flutter is an aeroelastic phenomenon in which the interaction of flowing air with aircraft surfaces (usually wings) results in a dynamic instability. In classical linear flutter, the wing's oscillations increase in amplitude until structural failure occurs (typically within a few cycles) [1, 2]. A number of modern aircraft, for example F-16s, have also experienced limit cycle oscillations

(LCOs) in which the wing's oscillation amplitude does not keep increasing, but instead settles at a constant value [3]. Nonlinearities in the system, such as geometric, aerodynamic, stiffness, or structural damping, act to limit the motion amplitude [4]. If the amplitude is large enough, the oscillatory motion can damage the wing/aircraft.

The aerospace industry worldwide is seeking to develop green aircraft which are cleaner, quieter and more efficient, based on demands for reduction of fuel burn, emission of pollutants and costs of operation. This has motivated studies into new aircraft designs and configurations by leading aircraft manufacturers such as Airbus, Boeing and Embraer. Most of these futuristic designs involve a higher level of structural flexibility than in conventional aircraft. Even currently, the trends in the aviation industry are to increase wing span (to reduce induced drag) and maximize use of composites, which lead to increased structural flexibility. Flexible aircraft structures result in the aeroelastic behavior becoming closer in frequency to that of the flight dynamics. Current procedures for flight control laws which are based on decoupling between flight dynamics (rigid-body) and aeroelastic dynamics, are thus not valid for flexible aircraft [5].

Flutter has typically been modeled with linear analysis, using linear aerodynamic theories such as those by Theodorsen [6, 7] and Wagner [8]. As LCOs are by their very nature nonlinear, these linear models are not capable of predicting all occurring LCOs and their features. This inability to fully predict LCOs creates the need for extensive flight testing, which is an expensive and time-consuming endeavor. These problems are present all the more in flexible aircraft like High Altitude Long Endurance (HALE) or futuristic aircraft with large aspect ratios. In these aircraft structures, the aeroelastic behavior may be strongly influenced by the flight dynamics. A nonlinear aeroelastic analysis tool capable of predicting all aspects of LCO behavior is hence desirable [9].

A combined formulation of aeroelasticity and flight dynamics, using Computational Fluid Dynamics (CFD) for aerodynamics and Finite Element Method (FEM) for structural dynamics is an expensive problem, requiring several hours of computational time even with High Performance Computing (HPC) resources. Hence semi-empirical methods such as the well-known Beddoes-Leishman [10] or ONERA dynamic stall model [11] are typically employed for inexpensive aeroelastic analysis in such regimes. While these are computationally fast, they do not provide insight into the flow phenomena and are only valid in regimes where they have been previously validated. Recognizing the need for a new class of low-cost, physics-based methods, many low-order unsteady flow solvers such as those by Ramesh et al. [12] and Eldredge & Wang [13] have been developed recently.

Structural nonlinearities in the aeroelastic system can arise from large deformations, material properties, or loose linkages [4]. The effects of structural nonlinearities on airfoil aeroelasticity, focusing on different types of nonlinear spring behavior such as bilinear or cubic variation in stiffness have been studied by several authors and are comprehensively reviewed in Lee et al. [4]. In these studies, it is assumed that the aerodynamics are linear, that is, the flow is incompressible, inviscid and attached to the airfoil. The onset and type of bifurcation, and the amplitude and frequency of the ensuing limit-cycle oscillations are investigated. Hard springs (positive cubic stiffening) are seen to result in a supercritical Hopf bifurcation, where LCOs occur only at freestream velocities greater than the linear flutter velocity and are independent of initial conditions. Soft springs (negative cubic stiffening) on the other hand, result in a subcritical Hopf bifurcation where LCOs may arise at velocities below the linear flutter velocity, and are dependent on the initial conditions. Further, chaotic oscillations are observed in a range

of freestream velocities for some configurations.

Aerodynamic nonlinearities may result from compressibility or viscous effects [4]. Tang et al. [14] have studied flutter and LCOs of 2D panels through linear theory and experiment, and concluded that there are significant differences between the two methods for large-amplitude LCOs owing to aerodynamic nonlinearities. Nonlinear aerodynamics resulting from viscous flow phenomena are largely dependent on the Reynolds number and the reduced frequencies involved, and leading-edge vortices (LEVs) have been seen to play a crucial role. In helicopter and wind-turbine applications, which are necessarily associated with large Reynolds numbers and low reduced frequencies, LEVs and the resulting dynamic stall phenomenon might lead to violent vibrations and mechanical failure [15]. Conversely, LEVs in high-frequency flows have been credited with contributing toward the success of high-lift flight in insects [16–19], and high propulsive [20] and power-extraction [21] efficiencies.

The type of nonlinearity in the system may result in either subcritical (below the flutter velocity) or supercritical (above the flutter velocity) LCOs. In structural nonlinearities for example, it is known that soft cubic stiffening results in subcritical LCOs that depend on initial conditions while hard cubic stiffening results in supercritical LCOs that are independent of initial conditions. In aerodynamic nonlinearities, Dowell and Tang [22] have reported that trailing-edge flow separation results in subcritical LCOs that depend on initial conditions. On the other hand, Ramesh et al. [23] have shown that 2D LEVs cause supercritical LCOs that are independent of initial conditions.

In this research, we are specifically concerned with aerodynamic nonlinearities and consequent limit-cycle oscillations resulting from leading-edge vortex shedding at low Reynolds numbers. In order to develop a suitable 3D low-order model for this regime, the nonlinearities in both fluid and structure must be suitably modeled for accurate prediction of LCOs in nonlinear aeroelastic systems [24]. The problem of a cantilevered flat plate undergoing LCOs has been well documented in the literature [25–27] and is used as a test case in this research for experiments and for development of a new 3D low-order model.

Ramesh et al. [28] have developed an unsteady airfoil theory based on potential flow, which holds valid uniformly regardless of amplitude and reduced frequency of motion, and shape of trailing wake. The method was seen to predict aerodynamic forces well even under conditions of large amplitude and high reduced frequency. To successfully model flows with leading edge vortices(LEVs), the Leading Edge Suction Parameter(LESP) was developed by Ramesh et al [29] to predict the onset of LEV formation. This parameter is a measure of the suction at the leading edge and it was shown that initiation of LEV formation always occurred at the same critical value of LESP, regardless of motion kinematics so long as the airfoil and Reynolds number of operation were the same. Using this criterion, a 2D discrete-vortex method was developed in which the LESP criterion was used to modulate the initiation, growth and termination of leading-edge vortices [12]. The method is abbreviated as LDVM (LESP-Modulated Discrete-Vortex Method).

In this paper, the 2D discrete-vortex method described above is first extended to 3D using a correction based on quasi-steady lifting line theory. This model is first validated against established potential flow methods. Then, it is validated against an experiment with a cantilevered flexible flat plate that undergoes prescribed oscillations. The flow physics in this regime are expected to be dominated by apparent-mass effects, large deflections and nonplanar wakes, flow

separation and LEV shedding. The ability of the model to account for these phenomena is discussed. Finally, an experiment with a cantilevered flexible flat plate is designed so as to exhibit high-frequency limit-cycle oscillations at speeds just above the flutter velocity, and results from post-flutter LCOs of the plate are presented.

2 METHODOLOGY

2.1 Numerical Model

The LDVM aerodynamic model which is based on the 2D discrete-vortex method is used as the basis for the numerical model employed in this research. The model is extended to 3D using a quasi-steady correction based on lifting line theory. The 2D LDVM method is first summarized below. The interested reader may refer to Refs. [12, 28] for further details.

2.1.1 LDVM: 2D discrete-vortex method

Large-angle unsteady thin-airfoil theory

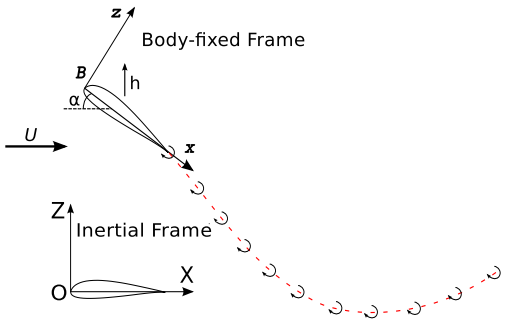

Figure 1: Depiction of time-stepping scheme.

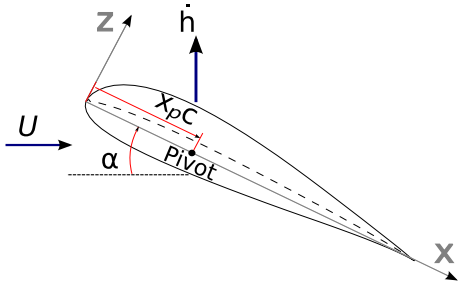

Figure 2: Airfoil velocities and pivot location.

At the foundation of the LDVM is a large-angle unsteady thin-airfoil theory detailed in Ramesh et al. [28]. This theory is based on the time-stepping formulation given by Katz & Plotkin [30], but eliminates the traditional small-angle assumptions in thin-airfoil theory which may be invalid in flows of current interest. At each time step, a discrete vortex is shed from the airfoil trailing edge (referred to as TEV) as depicted in figure 1. When dictated by the LESP-based shedding criterion (section 2.1.1), a discrete vortex is also shed from the leading edge at some time steps. The vorticity distribution over the airfoil at any given time step is taken to be a Fourier series truncated to r terms:

$$\gamma(\theta) = 2U \left[A_0 \frac{1+\cos\theta}{\sin\theta} + \sum_{i=1}^{r} A_i \sin(i\theta) \right] \tag{1}$$

where the transformation variable θ relates to the chordwise coordinate as: $x = c(1-\cos\theta)/2$, with x measured from the leading edge; that is, $0 \leq x \leq c$ and $0 \leq \theta \leq \pi$. A_0, A_1, ..., A_r are the time-dependent Fourier coefficients, and U is the freestream velocity. The Kutta condition (zero vorticity at the trailing-edge) is enforced implicitly through the form of the Fourier series. The Fourier coefficients are calculated by enforcing the boundary condition of zero normal flow

through the airfoil camberline as

$$A_0 = -\frac{1}{\pi}\int_0^\pi \frac{W(\theta)}{U}d\theta, \tag{2}$$

$$A_i = \frac{2}{\pi}\int_0^\pi \frac{W(\theta)}{U}\cos(i\theta)d\theta, \tag{3}$$

where $W(\theta)$ is the induced velocity normal to the airfoil camberline. This value is calculated from components of motion kinematics, depicted in figure 2, and induced velocities from all vortices in the flowfield.

When there is no LEV shedding in a time step, the only unknown is the strength of the last-shed trailing-edge vortex and this is calculated iteratively such that Kelvin's circulation condition is satisfied [28].

LESP criterion for LEV formation and shedding

The LESP is a measure of the suction peak at the leading edge, which in turn is caused by the stagnation point moving away from the leading edge when the airfoil is at an angle of attack. From Garrick [31] and von Kármán & Burgers [32], the suction at the leading edge in potential flow may be expressed as

$$S = \lim_{x\to LE}\frac{1}{2}\gamma(x)\sqrt{x}. \tag{4}$$

Evaluating using the current formulation, $S = \sqrt{c}UA_0$. The Leading Edge Suction Parameter is defined as a nondimensional value of suction at the leading edge, and is hence simply set equal to the first coefficient from Eq. (1), A_0.

As noted by Katz [33], real airfoils have rounded leading edges which can support some suction even when the stagnation point is away from the airfoil leading edge. The amount of suction that can be supported is a characteristic of the airfoil shape and Reynolds number of operation. When these quantities are constant, it was shown in Ramesh et al. [12] that initiation of LEV formation always occurred at the same value of LESP regardless of motion kinematics and history. This threshold value of LESP, which is a function of the airfoil shape and Reynolds number, is termed the critical LESP. This value, for any given airfoil and Reynolds number (and other specific operating conditions such as freestream turbulence and the presence of roughness), can be obtained from CFD or experimental predictions for a single motion [12], and can then be used for any other motion to predict LEV formation. In the LDVM model, a discrete vortex is shed is from the leading edge at those time steps when the instantaneous LESP (A_0 value) is greater than the critical LESP value. The strength of the LEV is determined such that the the instantaneous LESP value, which would have otherwise exceeded the critical LESP value, is made equal to the latter. This condition, along with Kelvin's condition, is used to determine shed vortex strengths iteratively in time steps where both TEV and LEV are shed. In this paper, we only use the LESP to predict LEV shedding and not to model it.

Vortex method details

In the current approach, the vortex-core model proposed by Vatistas et al. [34], which gives an excellent approximation to the Lamb-Oseen vortex, is used to represent the discrete vortices as

vortex blobs. Using this core model with order two, the velocities induced at X and Z (u and w) by the k^{th} vortex in the X and Z direction are:

$$[u, w] = \frac{\gamma_k}{2\pi} \frac{[(Z - Z_k), (X_k - X)]}{\sqrt{\left[(X - X_k)^2 + (Z - Z_k)^2\right]^2 + v_{core}^4}}. \tag{5}$$

Hald [35] has showed that the vortex-blob method is convergent (stable when run over long periods) so long as the vortex-core radius is larger than the average spacing between vortices. The average spacing between the vortices, d, is calculated as $d = c\Delta t^*$. The vortex core radius is taken to be approximately 1.3 times the average spacing between the vortices (as suggested by Leonard [36]): $v_{core} = 0.02c$. Convergence studies have been performed during the development of this method, and the numerical parameters have been selected such that the simulation results are not improved by either increasing or decreasing their values.

To control vortex count, and thus limit the computational cost, vortices which are a distance greater than ten chord lengths from the airfoil are deleted. When vortices are deleted from the domain, Kelvin's circulation condition which is used to iterate for shed vortex strengths is updated accordingly. Test simulations showed that results did not change when the cutoff distance was increased beyond ten chord lengths, implying that the velocity induced by vortices at a distance greater than ten chord lengths is negligible in comparison with other velocities acting on the airfoil.

2.1.2 Extension of discrete-vortex method to 3D

The classical lifting line theory is used in a quasi-steady sense in order to extend the LDVM to 3D for large aspect ratio unswept wings such as those considered in this research. The spanwise circulation distribution is modeled in the form of a Fourier series such that it goes to zero at the wingtips.

$$\Gamma(y) = 2bU\Sigma B_n \sin n\psi \tag{6}$$

where b is the wing span. The variation of circulation along the span results in vortex filaments being shed down the flow in accordance with Helmholtz theorem. The shed filament has a strength equal to the spanwise derivative of circulation distribution and results in upwash and downwash on the outboard and inboard wing sections respectively.

$$\frac{d\Gamma}{d\psi} = 2bU\Sigma n B_n \cos n\psi \tag{7}$$

The downwash at a specific spanwise station resulting from all the shed filaments is given by,

$$w_i = \int_{-b/2}^{b/2} \frac{d\Gamma}{y - y_o} = U\Sigma \frac{nB_n \sin n\psi}{\sin \psi} \tag{8}$$

This 3D downwash is is addition to the other components of downwash resulting from the wing motion and vortices in the flowfield (shown in figure 2). The influence of the 3D downwash on the 2D chordwise solutions are calculated using eqn. 3.

$$A_{0_{3D}} = -\Sigma \frac{nB_n \sin n\psi}{\sin \psi} \tag{9}$$

$$A_{1_{3D}} = A_{2_{3D}} = A_{n_{3D}} = 0 \tag{10}$$

Thus the only influence of the 3D downwash on the chordwise solution is on the A_0 term which is equivalent to an effective angle of attack and also serves to modulate LEV shedding. The chordwise circulation at each strip is now given by,

$$\Gamma(y) = Uc\pi(A_0 + A_{0_{3D}} + \frac{A_1}{2}) \tag{11}$$

Equating this equation for spanwise circulation with the assumed Fourier series distribution for circulation gives the lifting line equation.

$$\Sigma B_n \sin n\psi \left(\sin \psi + \frac{\pi n}{2AR}\right) = \frac{\pi \sin \psi}{2AR} \left(A_0 + \frac{A_1}{2}\right)_{2D} \tag{12}$$

This equation is solved at all spanwise locations in conjunction with the TEV strengths at each spanwise location through a Newton-Raphson iteration.

2.1.3 Limitations of the current approach

As shown in [12], the predictions from the current LDVM are in excellent agreement with those from CFD and experiments. Because the LDVM does not model thick or separated boundary layers, the method is restricted to motions where the LEV formation occurs without being accompanied by significant trailing-edge separation or stall. For most rounded-leading-edge airfoils, the LDVM is most reliable for high-reduced-frequency motions, with $k > 0.4$.

Another disadvantage, which is characteristic of vortex methods, is the exponential increase in computational time with number of vortices in the flow field ($\mathcal{O}(n^2)$). Fast summation methods [37], amalgamation of vortices, or deletion of vortices that exit the field of interest could be used to control the vortex count. As mentioned previously, vortices that are at a distance greater than ten chord lengths from the airfoil are deleted in the current implementation.

The lifting-line approach employed for the 3D correction in this paper is only valid for unswept, high-aspect ratio wings with planar wakes. Vortices shed for a spanwise station are assumed have a negligible effect on vortices shed from other spanwise stations. modeled. Further, the shedding of LEVs from the airfoil's leading edge is not modeled in this paper, though this may be implemented using the LDVM methodology outlined above.

Feature	Value	Unit
Wing chord	0.04	m
Wing span	0.35	m
Wing width	0.001	m
Wing mass	0.0472	kg
1st bending mode natural frequency	7.6394	Hz
Tip deflection during test	0.022	m
Angle of attack	8.0	deg
Freestream velocity	4.0	m/s

Table 1: Test parameters for prescribed motion of cantilevered flat plate.

2.2 Experiments

The focus of these experiments was to produce tests that generated aerodynamic nonlinearities by means of leading-edge vortex formation. Two tests were executed: the first test representing a prescribed movement with leading-edge vortex influence, and a the second test representing a flutter condition with limit-cycle oscillations. Both experiments were conducted on an open-section wind tunnel configuration with the wing positioned in the center of the flow with the desired angle of attack. The wing was attached to an aerodynamic balance capable of measuring forces in three directions. This balance is them connected to a signal conditioner device that amplifies the signal. The acquisition system was connected to a electrical no-break to prevent noise produced by the wind tunnel's inverter interfering with the results. Figure 3 shows a picture of the test setup.

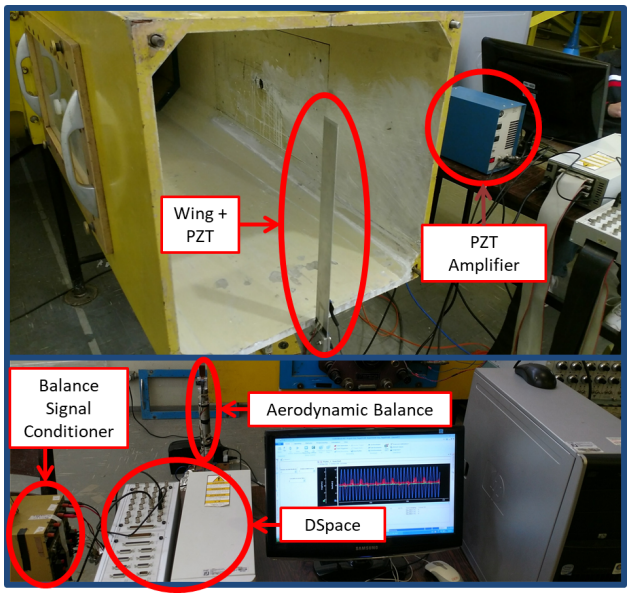

Figure 3: Test setup for experiments.

Before conducting the experiments, the aerodynamic balance was hooked up to the signal conditioner and characterized using standard weights ranging from 5g to 500g.

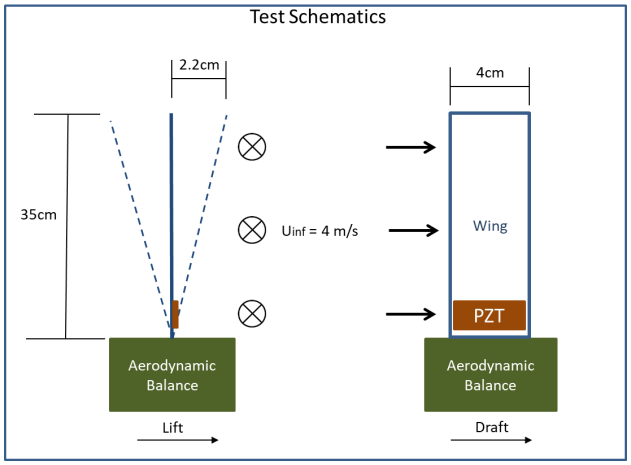

Figure 4: Depiction of prescribed movement of the cantilevered flat plate.

2.2.1 Prescribed oscillations

The prescribed movement test used a flat plate, positioned against a steady free-flow at a defined angle of attack. The fate plate was excited by PZTs attached to its root. These PZTs, when activated close to the plate's natural frequency for the first bending mode, generate high amplitude bending motion, that, with the freestream, produce an unsteady aerodynamic condition. Figure 4 shows a schematic of the test, and the relevant parameters are summarized in table 1.

The test results presented some noise compatible with the electrical grid. Figure 5 shows the frequency spectrum of the measured force signal.

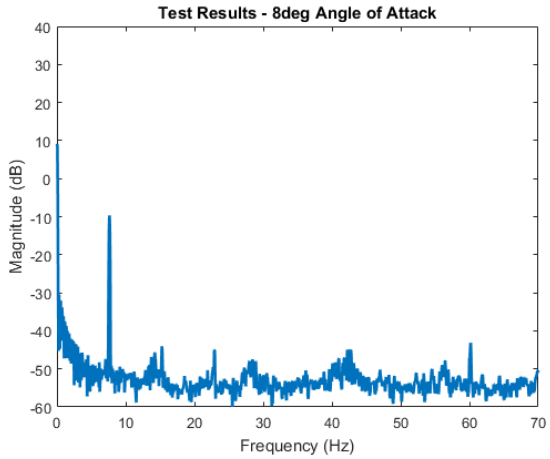

Figure 5: Frequency spectrum of force signal from the prescribed motion experiment.

To filter these results a moving median and a low-pass filter were used. Table 2 contains the parameters used in the filters.

The baseline measurements are used to measure the DC offset of the sensors. It is also used to quantify the delay between actuation on the PZT and wing movement. Figure 6 (left) shows the results from signal filtering.

Analyzing both baseline and lift signal it is possible to see in figure 6 (right) the average lift value for a steady 8 deg angle of attack, as well as the slight aerodynamic lag introduced by the flow, the reduced range between maximum and minimum is due to the reduced inertial forces,

Feature	Value	Unit
Moving Median Window	50	Samples
Filter Order	15	-
Cut-Off Frequency	12	Hz
Pass Band	1	dB

Table 2: Parameters used for filtering force signal.

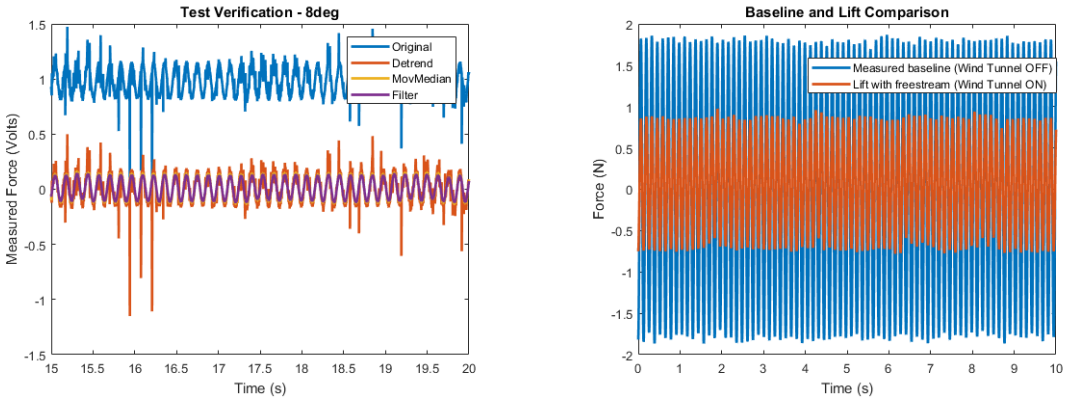

Figure 6: Force signal from experiment after filtering is applied (left), Comparison of baseline and processed force signal (right).

caused by the aerodynamic damping, and the generated lift that works against the inertial force.

2.2.2 Post-flutter limit-cycle oscillations

The Flutter condition test was designed to visualize Leading-Edge Vortexes influence when Limit-Cycle Oscillations are achieved. A more flexible flat plate, with a tip weight was used to achieve flutter in lower velocities, and the test consisted of increasing the tunnel velocity until flutter is achieved and Limit-Cycle Oscillations are sustained. Two configurations were tested by changing the tip weight position in regards to the center of chord. Table 3 details this experiment.

Feature	Value	Unit
Wing chord	0.026	m
Wing span	0.40	m
Wing width	0.0008	m
Wing mass	0.0257	kg
Angle of attack	0.0	deg
Tip mass	0.0328	kg
Tip mass position	0.003	m from center
Flutter velocity found	6.068	m/s
Tip mass	0.0328	kg
Tip mass position	0.006	m from center
Flutter velocity found	6.9305	m/s

Table 3: Test parameters for post-flutter limit-cycle oscillations of cantilevered flat plate

Feature	Value	Unit
Moving Median Window:	50	Samples
Filter Order:	15	-
Cut-Off Frequency:	55	Hz
Pass Band:	1	dB

Table 4: Parameters used for filtering force signal is post-flutter tests.

In both flutter results, noise was observed throughout the measurements, with the power spectrum showing several frequencies with similar magnitude.

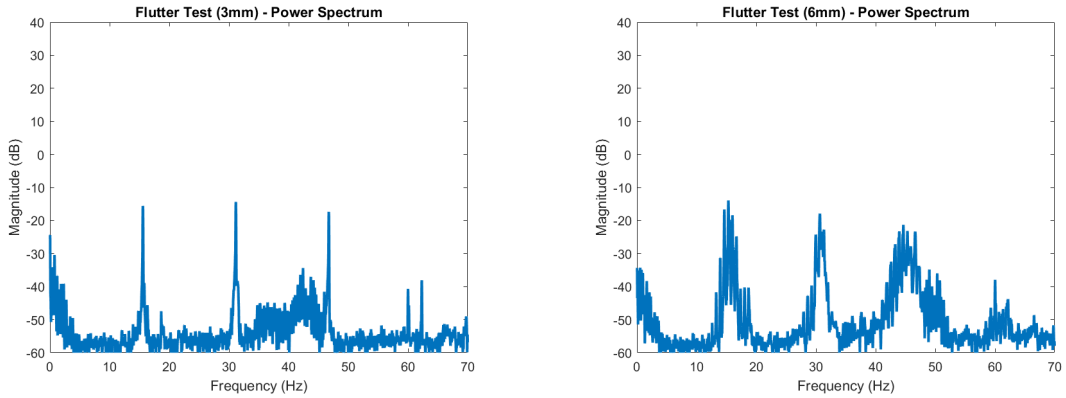

Figure 7: Power spectrum for measured force signal in post-flutter tests.

To filter these results, a moving median and a low-pass filter were used again. However, the cur-off frequency of the lowpass filter had to be changed to account for the other flexibility modes, that become stronger in flutter conditions. Table 4 contains the parameters used in the filters.

The baseline measurements are, again, used to measure the DC offset of the sensors. Figure 8 (left) shows the results from filtering the signal. By changing the position of the tip weight we were able to achieve a higher flutter velocity. Figure 8 (right) shows the results from filtering the second test signal.

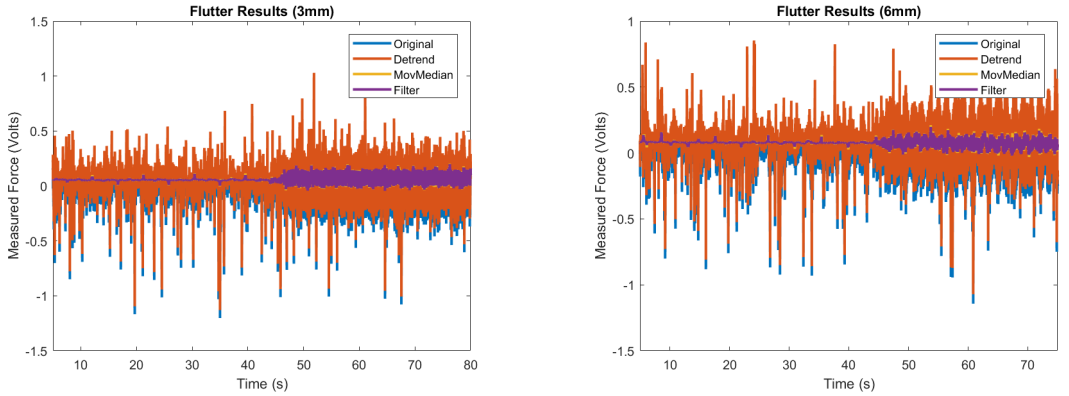

Figure 8: Comparison of baseline and processed force signal for the first (left) and second (right) flutter tests.

Feature	Value	Unit
Wing chord:	0.2	m
Wing span:	6	m
Wing section:	Flat plate	
Built incidence:	5	deg
Pitch-axis location	0.25	
Reduced frequency	0.0558	
Freestream velocity:	10.0	m/s

Table 5: Test parameters for validation of low-order model against DBL.

3 RESULTS AND DISCUSSION

In this section, the newly developed low-order model is first validated against an established potential-flow method. The model is then used the study the same kinematics as the prescribed-oscillation experiment described in table 1, and results from the two methods are compared. Finally post-flutter limit-cycle oscillations of the plate are studied using experiment.

3.1 Validation and demonstration of low-order model

A planar high-aspect-ratio wing undergoing oscillations in pitch is considered for validation and demonstration of the low-order model developed in this research. Validation is carried out against the doublet-lattice method (DBL) [38] which is a well-established tool for aerodynamic (potential flow) prediction of such scenarios. The parameters used in the simulation are listed in table 5.

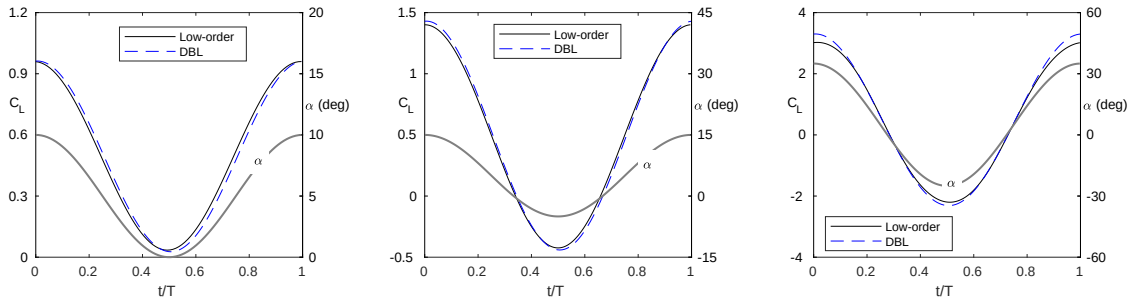

Figure 9: Comparison of lift coefficient prediction between the low-order model and DBL for three pitching kinematics of amplitudes 5, 10 and 30 deg (from left to right).

Figure 9 shows the comparison of lift coefficient between the two methods for oscillation amplitudes of 5, 10 and 30 deg (left to right). For low amplitudes of motion (5 deg and 10 deg), we see an excellent match between the two methods. This confirms that the newly developed low-order model is able to successfully account for 3D effects through the quasi-steady lifting line approximation. For the higher amplitude of 30 deg, the prediction from the low-order model is lower than that from DBL. This is expected, as the DBL is a linear method that is inaccurate at high angles of attack, whereas the current model account for nonlinearity from high angles of attack.

Figure 10 shows the nondimensional spanwise circulation distribution on the wing, at the beginning of the oscillation cycle and halfway through the oscillation cycle (left and right respec-

tively). The figure shows the expected circulation distribution for a rectangular high-aspect ratio wing, peaking at the root and going to zero at the wingtips.

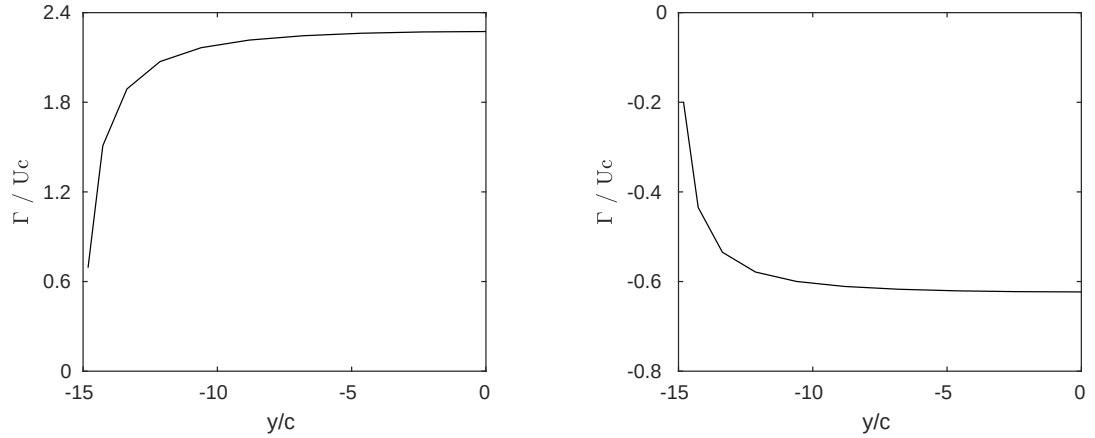

Figure 10: Comparison of circulation distribution on the wing at $t^*/T^* = 0.0$ (left) and $t^*/T^* = 0.5$ (right).

Figure 11 shows the distribution of LESP across the wing span, at the beginning of the oscillation cycle and halfway through the oscillation cycle (left and right respectively). The critical LESP which indicates LEV shedding (taken equal to 0.11 for a flat plate [12]) is also marked on these plots. At $t^*/T^* = 0$, we see that the LESP is greater than the $LESP_{crit}$ on almost the full span. At $t^*/T^* = 0.5$, the LESP is negative, but doesn't cross the $LESP_{crit}$ value. From these plots, we can conclude that LEV shedding on the upper wing surface is expected for part of the oscillation cycle.

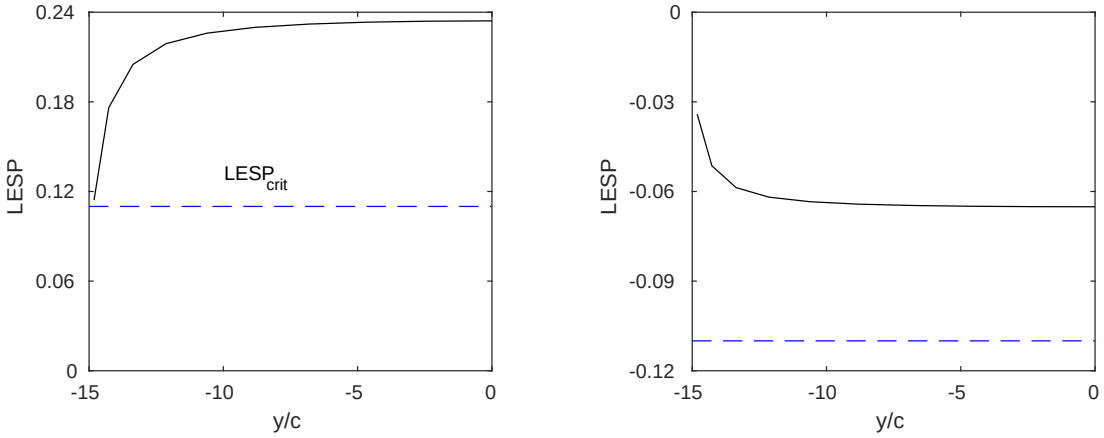

Figure 11: Comparison of LESP distribution on the wing at $t^*/T^* = 0.0$ (left) and $t^*/T^* = 0.5$ (right). Dashed blue line shows the critical LESP value denoting LEV formation.

Figure 12 shows the vorticity in the wake, at the beginning of the oscillation cycle and halfway through the oscillation cycle (top and bottom respectively). The wake shows insignificant rollup, which is expected for the low reduced frequency considered in this case.

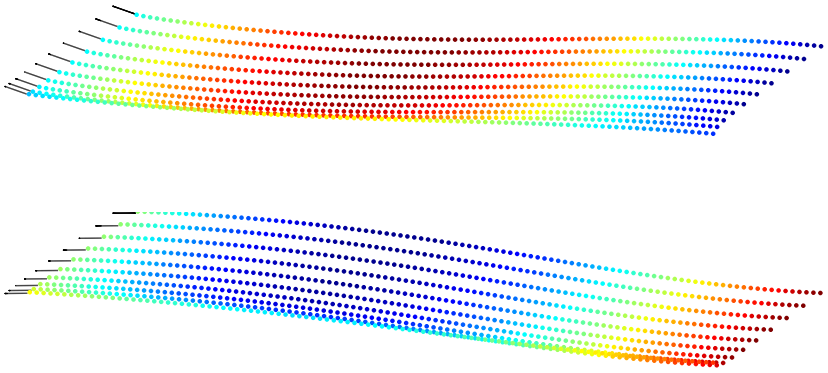

Figure 12: Comparison of wake vorticity at $t^*/T^* = 0.0$ (top) and $t^*/T^* = 0.5$ (bottom).

3.2 Prescribed oscillations

In this section, the experiment described in table 1 is presented along with results from the low-order method.

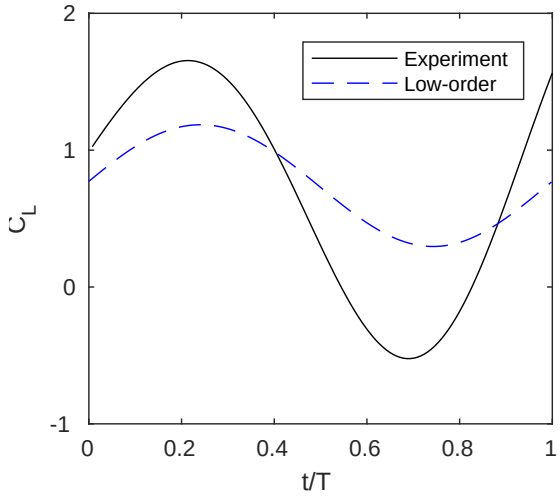

Figure 13: Test setup for experiments.

Figure 13 shows comparison of lift coefficient between the experiment and low-order model. We note that there is a level of uncertainty in the experiment, owing to the method used to remove the inertial loads. The general trend in lift is seen to agree, though the peak amplitudes of lift from experiment are significantly higher than those from the numerical model. Results from the low-order model are analyzed in further detail below.

Figure 14 shows the nondimensional spanwise circulation distribution on the wing, at the beginning of the oscillation cycle and halfway through the oscillation cycle (left and right respectively).

Figure 15 shows the distribution of LESP across the wing span, at the beginning of the oscillation cycle and halfway through the oscillation cycle (left and right respectively). The critical LESP which indicates LEV shedding (taken equal to 0.11 for a flat plate [12]) is also marked on

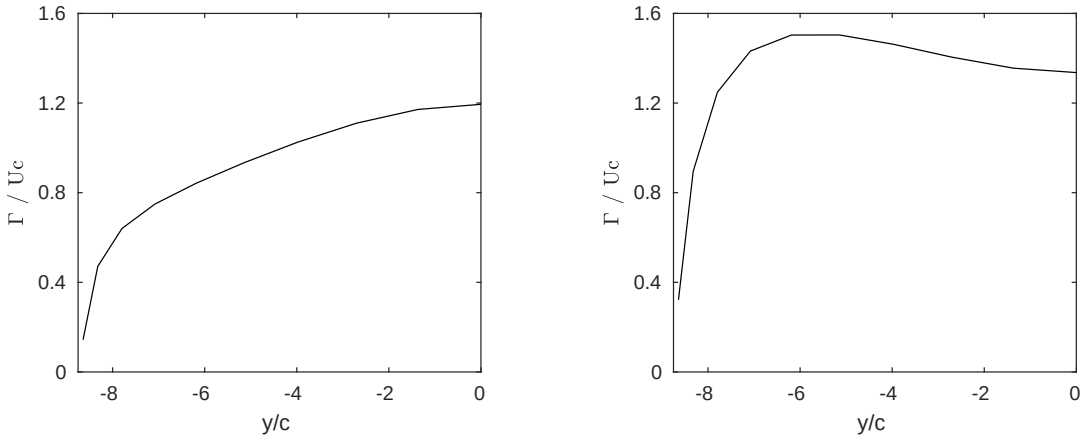

Figure 14: Comparison of circulation distribution on the wing at $t^*/T^* = 0.0$ (left) and $t^*/T^* = 0.5$ (right).

these plots. We see that at both instants during the cycle, the LESP value on almost the whole wing is higher than $LESP_{crit}$. This indicates the aerodynamics is dominated by LEV formation and shedding, which must be model led for better prediction by the numerical method.

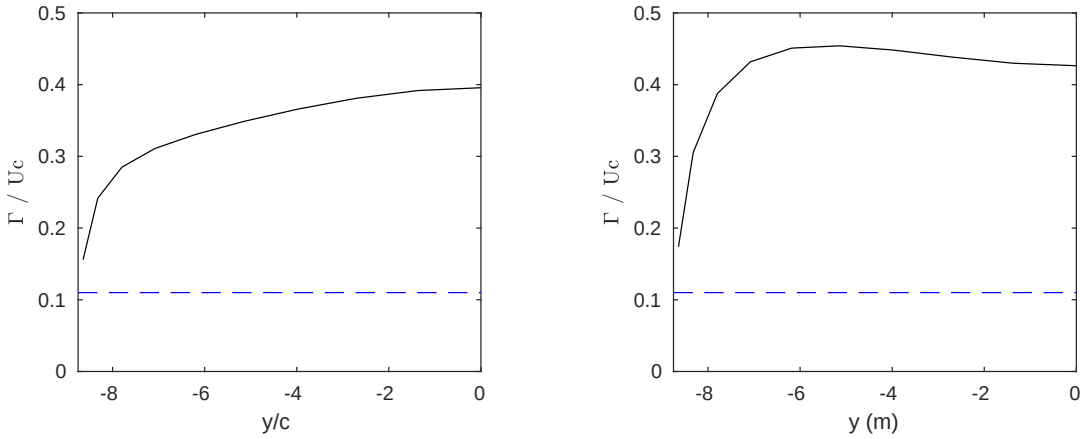

Figure 15: Comparison of LESP distribution on the wing at $t^*/T^* = 0.0$ (left) and $t^*/T^* = 0.5$ (right). Dashed blue line shows the critical LESP value denoting LEV formation.

Figure 16 depicts the vorticity in the wake, at the beginning of the oscillation cycle and halfway through the oscillation cycle (top and bottom respectively). In this case, the wake shows a higher degree of deformation owing to the different type of motion (bending as opposed to pitching) and the higher reduced frequency.

3.3 Post-flutter limit-cycle oscillations

The final results from the post-flutter experiment, after applying the appropriate filters, are presented here. In both cases, we clearly see evidence of persistent limit-cycle behavior after the flutter velocity is reached. Small deformations were registered, pointing to a structural behavior still in the linear regime. The oscillations however were not of the same amplitude and period as expected. Noise presents a significant problem for this case, and mechanisms

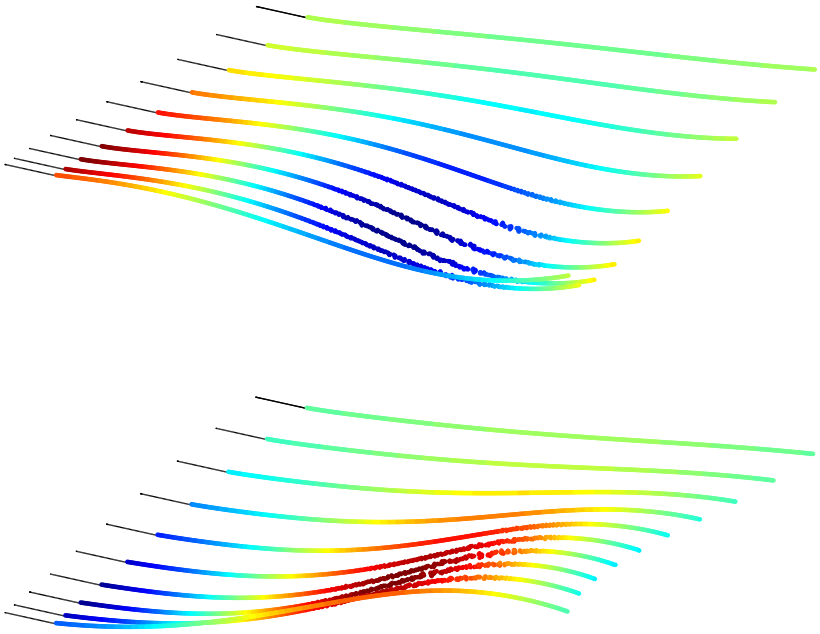

Figure 16: Comparison of wake vorticity at $t^*/T^* = 0.0$ (top) and $t^*/T^* = 0.5$ (bottom).

to reduce this will be studied in future research. The preliminary results point to the presence of significant aerodynamic nonlinearities associated with flow separation and LEV shedding, which much be accounted for in numerical models to simulate all limit-cycle characteristics of the system.

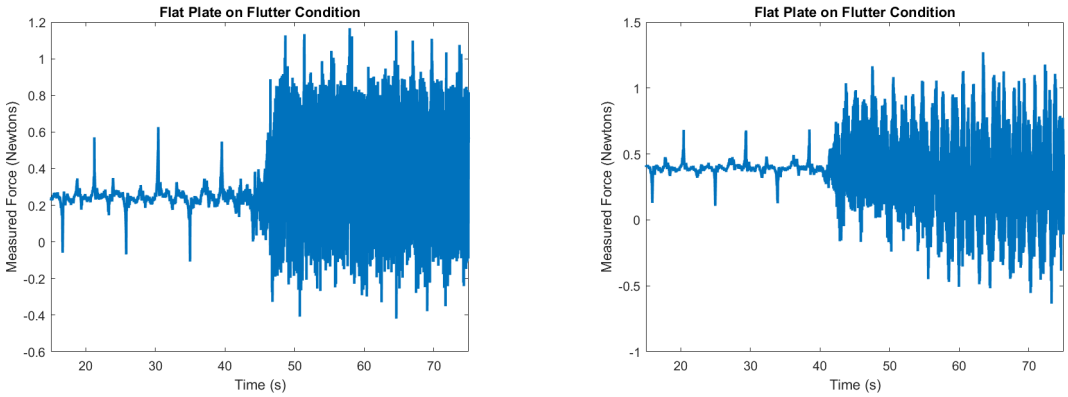

Figure 17: Post-flutter limit-cycle oscillations observed in the two experiments.

4 CONCLUSIONS

Aeroelastic behavior of a cantilevered flat plate in a low Reynolds number regime is studied numerically and experimentally in this paper. Experiments were developed for the case of the plate undergoing prescribed oscillations, and for the case of the plate undergoing post-flutter limit-cycle oscillations. A new low-order numerical model based on a quasi-steady lifting-line correction to the LDVM discrete-vortex method was developed. This model was seen to successfully account for nonlinearites such as nonplanar wake structures and large oscillation amplitudes. The model was also capable of predicting the occurrence of LEV formation over the wing surface using the LESP theory. The prescribed oscillation experiment was compared against the

newly developed numerical model. The results indicated that additional aerodynamic nonlinearities such as leading-edge vortex shedding and trailing-edge flow separation must also be modeled to achieve accurate results in this regime. The post-flutter experiment showed limit-cycle oscillations, through they were not single-period and were influenced by noise. A more precise experiment for post-flutter LCOs, as well as modifications to the low-order model to account for flow separation and LEV shedding will be developed in future research.

5 ACKNOWLEDGMENTS

The authors gratefully acknowledge the support of the Newton Fund, under the Newton Research Collaboration Programme, reference NRCP1516/4/26.

6 REFERENCES

[1] Bisplinghoff, R. L. and Ashley, H. (1996). *Aeroelasticity*. Courier Dover Publications.

[2] Fung, Y. (2002). *An introduction to the theory of aeroelasticity*. Courier Dover Publications.

[3] Bunton, R. W. and Denegri, C. M. (2000). Limit cycle oscillation characteristics of fighter aircraft. *Journal of Aircraft*, 37(5), 916–918.

[4] Lee, B. H. K., Price, S. J., and Wong, Y. S. (1999). Nonlinear aeroelastic analysis of airfoils: bifurcation and chaos. *Progress in Aerospace Sciences*, 35(3), 205–334.

[5] Silvestre, F. J., Guimarães Neto, A. B., Bertolin, R. M., et al. (2016). Aircraft control based on flexible aircraft dynamics. *Journal of Aircraft*.

[6] Theodorsen, T. (1935). General theory of aerodynamic instability and the mechanism of flutter. NACA Rept. 496.

[7] Theodorsen, T. and Garrick, I. E. (1942). Flutter calculations in three degrees of freedom. NACA Rept. 741.

[8] Wagner, H. (1925). Über die Entstehung des dynamischen Auftriebes von Tragflügeln. *ZaMM*, 5(1), 17–35.

[9] Denegri, C. M., Dubben, J. A., and Maxwell, D. L. (2005). In-flight wing deformation characteristics during limit cycle oscillations. *Journal of Aircraft*, 42(2), 500–508.

[10] Leishman, J. G. and Beddoes, T. S. (1989). A semi-empirical model for dynamic stall. *Journal of the American Helicopter Society*, 34(3), 3–17.

[11] Petot, D. (1983). Progress in the semi-empirical prediction of the aerodynamic forces due to large amplitude oscillations of an airfoil in attached or separated flow. Tech. Rep. 1983-111.

[12] Ramesh, K., Gopalarathnam, A., Granlund, K., et al. (2014). Discrete-vortex method with novel shedding criterion for unsteady airfoil flows with intermittent leading-edge vortex shedding. *Journal of Fluid Mechanics*, 751, 500–538.

[13] Wang, C. and Eldredge, J. D. (2012). Low-order phenomenological modeling of leading-edge vortex formation. *Theoretical and Computational Fluid Dynamics*, 27(5), 577–598.

[14] Tang, D. M., Yamamoto, H., and Dowell, E. H. (2003). Flutter and limit cycle oscillations of two-dimensional panels in three-dimensional axial flow. *Journal of Fluids and Structures*, 17(2), 225–242.

[15] Leishman, J. G. (2002). *Principles of Helicopter Aerodynamics*. Cambridge Aerospace Series.

[16] Ellington, C. P. (1995). Unsteady aerodynamics of insect flight. In *Symposia of the Society for Experimental Biology*, vol. 49. p. 109.

[17] Shyy, W. and Liu, H. (2007). Flapping wings and aerodynamic lift: The role of leading-edge vortices. *AIAA Journal*, 45(12).

[18] Ellington, C. P. (1999). The novel aerodynamics of insect flight: applications to micro-air vehicles. *Journal of Experimental Biology*, 202(23), 3439–3448.

[19] Dickinson, M. H. and Gotz, K. G. (1993). Unsteady aerodynamic performance of model wings at low Reynolds numbers. *Journal of Experimental Biology*, 174(1), 45–64.

[20] Anderson, J., Streitlien, K., Barrett, D., et al. (1998). Oscillating Foils of High Propulsive Efficiency. *Journal of Fluid Mechanics*, 360(1), 41–72.

[21] Kinsey, T. and Dumas, G. (2008). Parametric study of an oscillating airfoil in a power-extraction regime. *AIAA Journal*, 46(6), 1318–1330.

[22] Dowell, E. H. and Tang, D. (2002). Nonlinear aeroelasticity and unsteady aerodynamics. *AIAA journal*, 40(9), 1697–1707.

[23] Ramesh, K., Murua, J., and Gopalarathnam, A. (2015). Limit-cycle oscillations in unsteady flows dominated by intermittent leading-edge vortex shedding. *Journal of Fluids and Structures*, 55, 84–105.

[24] Sheta, E. F., Harrand, V. J., Thompson, D. E., et al. (2002). Computational and experimental investigation of limit cycle oscillations of nonlinear aeroelastic systems. *Journal of Aircraft*, 39(1), 133–141.

[25] Tang, D., Dowell, E. H., and Hall, K. C. (1999). Limit cycle oscillations of a cantilevered wing in low subsonic flow. *AIAA journal*, 37(3), 364–371.

[26] Ghadiri, B. and Razi, M. (2007). Limit cycle oscillations of rectangular cantilever wings containing cubic nonlinearity in an incompressible flow. *Journal of Fluids and Structures*, 23(4), 665–680.

[27] Tang, L., Païdoussis, M. P., and Jiang, J. (2009). Cantilevered flexible plates in axial flow: energy transfer and the concept of flutter-mill. *Journal of Sound and Vibration*, 326(1), 263–276.

[28] Ramesh, K., Gopalarathnam, A., Edwards, J. R., et al. (2013). An unsteady airfoil theory applied to pitching motions validated against experiment and computation. *Theoretical and Computational Fluid Dynamics*, 27(6), 843–864.

[29] Ramesh, K., Gopalarathnam, A., Ol, M. V., et al. (2011). Augmentation of inviscid airfoil theory to predict and model 2D unsteady vortex dominated flows. AIAA Paper 2011–3578. In review with *AIAA Journal*.

[30] Katz, J. and Plotkin, A. (2000). *Low-Speed Aerodynamics*. Cambridge Aerospace Series.

[31] Garrick, I. E. (1937). Propulsion of a flapping and oscillating airfoil. NACA Rept. 567.

[32] von Kármán, T. and Burgers, J. M. (1963). *General Aerodynamic Theory - Perfect Fluids*, vol. 2 of Aerodynamic theory: a general review of progress. Durand, W. F. , Dover Publications.

[33] Katz, J. (1981). Discrete vortex method for the non-steady separated flow over an airfoil. *Journal of Fluid Mechanics*, 102(1), 315–328.

[34] Vatistas, G. H., Kozel, V., and Mih, W. C. (1991). A simpler model for concentrated vortices. *Experiments in Fluids*, 11(1), 73–76.

[35] Hald, O. H. (1979). Convergence of vortex methods for Euler's equations, II. *SIAM Journal on Numerical Analysis*, 16(5), 726–755.

[36] Leonard, A. (1980). Vortex methods for flow simulation. *Journal of Computational Physics*, 37(3), 289–335.

[37] Carrier, J., Greengard, L., and Rokhlin, V. (1988). A fast adaptive multipole algorithm for particle simulations. *SIAM Journal on Scientific and Statistical Computing*, 9(4), 669–686.

[38] Albano, E. and Rodden, W. P. (1969). A doublet-lattice method for calculating lift distributions on oscillating surfaces in subsonic flows. *AIAA journal*, 7(2), 279–285.

COPYRIGHT STATEMENT